Reaction Chemistry & Engineering

ROYAL SOCIETY OF CHEMISTRY

PAPER

View Article Online
View Journal | View Issue

Cite this: *React. Chem. Eng.*, 2020, 5, 1939

Mesoporous silica-encapsulated gold core–shell nanoparticles for active solvent-free benzyl alcohol oxidation†

Ellis Hammond-Pereira,[a] Kristin Bryant,[a] Trent R. Graham,[ab] Chen Yang,[ac] Sebastian Mergelsberg,[b] Di Wu[acde] and Steven R. Saunders *[ad]

Received 18th May 2020,
Accepted 18th August 2020

DOI: 10.1039/d0re00198h

rsc.li/reaction-engineering

Silica-encapsulated gold core@shell nanoparticles (Au@SiO_2 CSNPs) were synthesized *via* a tunable bottom-up procedure to catalyze the aerobic oxidation of benzyl alcohol. The nanoparticles exhibit a mesoporous shell which enhances selectivity by inhibiting the formation of larger species. Adding potassium carbonate to the reaction increased conversion from 17.3 to 60.4% while decreasing selectivity from 98.4 to 75.0%. A gold nanoparticle control catalyst with a similar gold surface area took 6 times as long to reach the same conversion, achieving only 49.4% selectivity. These results suggest that the pore size distribution within the inert silica shell of Au@SiO_2 CSNPs inhibits the formation of undesired products to facilitate the selective oxidation of benzaldehyde despite a basic environment. A smaller activation energy, mass transport analysis, and mesopore distribution together suggest the Au@SiO_2 CSNP catalyst demonstrates higher activity through beneficial in-pore orientation, promoting a lower activation energy mechanistic pathway. Taken together, this is a promising catalytic structure to optimize oxidation chemistries, without leveraging surface-interacting factors like chelating agents or active support surfaces.

1. Introduction

Oxidation is an essential step in many organic syntheses, used for petrochemicals,[1] pharmaceuticals,[2] food additives[3] and others.[4] The selective oxidation of alcohols to aldehydes is specifically studied due to the reaction's thermodynamic preference for further oxidation to the carboxylic acid and ester products.[1] Aerobic oxidation has risen in popularity as a green alternative to using stronger oxidizing agents,[5] producing easily separable byproducts: water and hydrogen. There exists a need for a catalyst that can perform aerobic oxidations selectively by halting the reaction before reaching the fully oxidized product. While homogeneous catalysts exhibit high tunability through selection of complexing ligands,[6–9] heterogeneous catalysts are much simpler to separate from the reaction mixture, making them more practical for large-scale catalysis.[10] This ease of separation comes at the cost of performance; heterogeneous catalysts suffer from a trade-off between selectivity, reactivity, and recyclability.[11] In practice, literature studies aim to improve the typically low reactivity associated with selective oxidation through the use of weak oxidizing agents and bases.

Benzyl alcohol oxidation (Scheme 1) is commonly used as a test reaction for oxidizing catalysts due to the potential for selectivity among multiple undesired products and low activity on gold in the absence of a base.[12] To remedy the low activity, a base is often added to the reaction, typically to the severe detriment of selectivity towards the aldehyde product.[13,14] To mitigate this trade-off between activity and selectivity, many studies have pursued interacting support materials and bimetallic active surfaces. Higher reactivity and selectivity has been attained using chemically active supports such as ceria,[14,15] silica–noble metal complexes,[16] and oxides of transition metals, lanthanides, and actinides.[17–19] Because of the complexity of active phase-support interfaces, understanding the precise mechanistic behavior of benzyl alcohol oxidation on state-of-the-art heterogeneous catalysts is difficult.

The interfacial effects between the support and active surface are further complicated by the use of a bimetallic catalyst,[20–23] where both metal–metal and metal–support interactions must be accounted for.[24] Recent studies

[a] *The Gene and Linda Voiland School of Chemical Engineering and Bioengineering, Washington State University, Pullman, Washington 99164, USA.*
E-mail: steven.r.saunders@wsu.edu
[b] *Pacific Northwest National Laboratory, Richland, Washington 99352, USA*
[c] *Alexandra Navrotsky Institute for Experimental Thermodynamics, Washington State University, Pullman, Washington 9916, USA*
[d] *Department of Chemistry, Washington State University, Pullman, Washington 99164, USA*
[e] *Materials Science and Engineering, Washington State University, Pullman, Washington 99163, USA*

† Electronic supplementary information (ESI) available. See DOI: 10.1039/d0re00198h

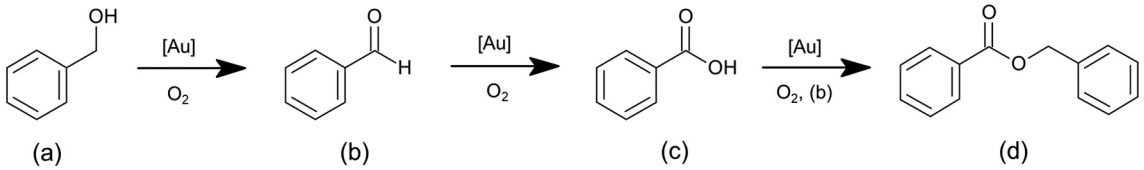

Scheme 1 Sequential oxidations of (a) benzyl alcohol into (b) benzaldehyde, (c) benzoic acid, and (d) benzyl benzoate.

evaluated the impregnation of gold into zeolites using chelating agents to anchor metal nanoparticles in place within pores.[25–28] Others have used chelating polymer surfaces that show increased activity and extreme recyclability by preventing nanoparticle aggregation but prove difficult for fundamental research due to the nature of chelation.[23] The chelating agents inhibit leaching of the active metal phase into the solution; however, these anchoring species interact with the gold surface: reducing the number of active sites, limiting access to reactive sites, or influencing catalytic behavior. The necessity of chelating agents for synthesis renders their impact both unpredictable and immeasurable. Additionally, the zeolite impregnation method prevents the formation of nanoparticles larger than the pore it grows within. As a result, the ways impregnated zeolite catalysts can be tuned to leverage diffusion effects is fundamentally limited by their top-down synthesis.

An alternative to anchoring catalytically active species *via* encapsulation in an unstructured porous framework synthesized in a bottom-up manner to improve tunability is proposed in this work. Gold nanoparticles are encapsulated by mesoporous silica (Au@SiO_2) to improve the stability of the active phase without the use of permanent anchoring agents. CTAB-stabilized gold nanoparticles allow silica to condense around each nanoparticle, rather than agglomerating into a bulk support material. Due to the individual encapsulation, the stabilizing surfactant can then be removed *via* calcination without significant nanoparticle growth. The core–shell structure of the catalyst was characterized using transmission electron microscopy (TEM), adsorbed-gas nonlocal density functional theory (NL-DFT), inductively coupled plasma-mass spectrometry (ICP-MS), coupled thermogravimetric analysis and mass spectrometry (TGA-MS), and high-energy X-ray diffraction (heXRD), with particular focus on tracing the enhanced activity and selectivity of benzyl alcohol oxidation in alkaline conditions. The ease of tailoring the physical properties of the supporting silica characteristics will lead to a uniquely flexible platform for future catalytic studies, where the concept of physically enforced selectivity and activity can be further explored.

2. Experimental

2.1 Materials

Reagents were used as received and without further alteration or purification. Benzyl alcohol (BnOH, ≥99.0%), biphenyl (99.0%), benzaldehyde (BzH, ≥99.0%), benzyl benzoate (BnBzO, ≥99.0%), benzoic acid (BzOH, 99.5%), cerium(IV) oxide (CeO_2, 99.99%, 14 micron powder), silica (SiO_2; 0.060–0.2 mm), and potassium carbonate (K_2CO_3, ≥99.0%) were purchased from Alfa Aesar. Tetrachloroauric(III) acid trihydrate ($HAuCl_4{\cdot}3H_2O$, ≥49.0% Au), and sodium borohydride ($NaBH_4$, 99.0%) were acquired from ACROS Organics. Cetyltrimethylammonium bromide (CTAB, 100%) was obtained from Chem-impex Int'l Inc, ethanol (anhydrous) from Decon Laboratories, nitric acid (TraceMetal Grade) and toluene (99.9%) from Fischer Scientific, hydrochloric acid (HCl, 36.5–38.0%) and *n*-hexane (C_6H_{14}; >95%) from J.T. Baker, sodium hydroxide (NaOH, ≥98.0%) from Macron Chemicals, tetraethyl orthosilicate (TEOS) (99.0%) and from Aldrich, and clinical laboratory reagent grade water (CLRW) from Thermo Scientific.

2.2 Nanoparticle synthesis

Core–shell nanoparticles were synthesized using a modified procedure from Chen *et al.*[29] The described synthesis was modified by the replacement of (3-aminopropyl) triethoxysilane with a second addition of tetraethyl orthosilicate. This prevented the formation of an internal cavity, yielding a core–shell structure as opposed to a yolk–shell structure.[29] To begin the synthesis, 10 mL of 0.5 M aqueous NaOH was added to 240 mL of 5.7 mM aqueous CTAB. The mixture was stirred at 80 °C for 20 minutes prior to increasing the temperature to 90 °C. Three prepared solutions then were added in quick succession: Firstly, 10 mL of 1.0 M aqueous $HAuCl_4{\cdot}3H_2O$, followed by 3 mL of 1.0 M aqueous $NaBH_4$ (to form the gold nanoparticle cores), and finally 22 mL of 0.4 M ethanolic solution of TEOS (to encapsulate the gold nanoparticles in silica *via* the Stöber process). The mixture was stirred for 40 minutes prior to the addition of 27.4 mL of 1.2 M ethanolic solution of TEOS. The core–shell nanoparticles were then stirred at 90 °C for 8 hours to etch the silica, adding water to maintain the volume. The etched nanoparticles were collected *via* vacuum filtration, washed with ethanol, and dried for 12 hours at 40 °C under vacuum (340 mbar). The nanoparticles were calcined at a rate of 10 °C min^{-1} to 600 °C to clear the pores and gold surface of organic material.

Silica-supported gold nanoparticles (Au–SiO_2 NPs) and ceria-supported gold nanoparticles (Au–CeO_2 NPs) were synthesized using a silylamine reversible ionic liquid *via* a modified procedure,[30–32] for use as control catalysts. The synthesis of the reversible ionic liquid is detailed in the ESI,† page S2. Briefly, 0.0298 g of $HAuCl_4$ and 20 mL of hexane were added to 3.975 g of 3-aminopropyltriethylsilane (APTES)

ionic liquid and the mixture stirred until the gold precursor had completely dissolved. 400 μL of 0.1 M aqueous $NaBH_4$ was added to the reaction solution while stirring at 300 rpm. The reaction was stirred for 1 hour. The gold nanoparticles were deposited onto ceria and non-porous silica following a method demonstrated previously by Bryant *et al.*[31,32] For each deposition, 8 mL of the as-synthesized nanoparticle solution was added to a flask containing 100 mL of hexane and roughly 12 g of silica gel or ceria while stirring at 400 rpm. The flask was connected to a reflux column and the temperature was brought to reflux conditions (~69 °C). Refluxing continued until the deposition was complete, indicated by a color change of the support from white to purple (~20 min). The supernatant was discarded and the supported nanoparticles were washed with hexane then dried for 12 hours at 40 °C under vacuum (340 mbar). The catalysts were calcined at a rate of 10 °C min^{-1} to 600 °C to remove the silane species from the support surface.

2.3 Catalyst characterization

Nanoparticle morphology was analyzed using transmission electron microscopy. The nanoparticles were suspended in toluene (2 mg catalyst/mL toluene). A 3 μL aliquot was deposited on a 200 mesh formvar/carbon TEM grid and dried overnight at 40 °C under vacuum (340 mbar). The transmission electron microscope (FEI Tecnai T20) was operated at 200 kV and ImageJ (version 1.52a) was utilized to analyze the micrographs.

Metal loading was determined *via* inductively coupled plasma-mass spectrometry (ICP-MS) on an Agilent 770 mass spectrometer. Nanoparticle samples (4, 6, and 8 mg) were digested in 2.4 mL aqua regia (1 : 3 nitric acid : hydrochloric acid) in sealed pressure vessels, stirred at 600 rpm overnight. The samples were diluted one hundredfold in high purity water before analysis.

Organic compositions were analyzed *via* thermogravimetric analysis-coupled mass spectrometry (TGA-MS). As-synthesized CSNPs were loaded into a STA 449 F5 Jupiter for thermogravimetric analysis, wherein the evolved gas was directly transferred into a QMS 403 D Aëolos mass spectrometer. The sample was heated from 30 °C to 600 °C at a rate of 10 °C min^{-1} in air. The procedure was repeated for CSNPs after use in one reaction. Calcination studies on both control catalysts were conducted using TGA without mass spectrometry. Bulk catalyst calcination was conducted under the same conditions in an oven.

Pore size analysis of core–shell nanoparticles was conducted using a Micromeritics 3Flex surface physisorption characterization analyzer. N_2 adsorption/desorption was conducted up to 1.0 atm. The results were used to calculate pore size distribution using nonlocal density functional theory.[33]

Fourier transform infrared spectroscopy (FTIR) was conducted on CSNPs using a Thermo Scientific Nicolet iS10 IR spectrometer. Catalyst samples were mixed with potassium bromide, compressed into a pellet, and analyzed *via* transmission FTIR. CTAB, benzyl alcohol, benzaldehyde, and benzyl benzoate were analyzed using the same method to be used as standards.

The evolution of the gold nanoparticle core and mesoporous silica shell during the synthesis was also investigated using high-energy X-ray diffraction (HeXRD). HeXRD was conducted on core–shell nanoparticle samples taken before the second addition of TEOS, after synthesis but prior to calcination, and after calcination. Data for high energy x-ray diffraction and total x-ray scattering for PDF analysis was collected at beamline 11 ID-B of the Advanced Photon Source,[34] Argonne National Laboratory. Detailed methodology is available in the ESI,† page S3.

2.4 Reaction conditions

2.4.1 Standard reaction conditions. The standard neat reaction conditions are as follows: in a 9 mL sealed glass reaction vessel, a stock solution containing 9.6 mmol benzyl alcohol (limiting reagent) and 10 μmol biphenyl (internal standard) was added to 0.5 μmol of gold, with the actual of mass catalyst added depending on gold loading (43.4 mg CSNPs, 175.1 mg Au–SiO_2, or 95.0 mg Au–CeO_2). Reactions were performed with and without a base (130 mg K_2CO_3 added, before the stock solution). Vessels containing all species were sonicated for 1 minute, then attached to a pressurized O_2 tank. To purge the headspace, the pressure was raised to 6 bar and allowed to equilibrate before venting. The pressurization/venting cycle was repeated 3 times in total. Once lowered to atmospheric pressure (~99.7% O_2), The vessel was then submerged in a 100 °C oil bath and magnetically stirred at 600 rpm. After 3 minutes of thermal equilibration, the atmosphere was raised to 6 bar (final headspace >99.9% O_2) and allowed to react for 1 hour. The reactions were quenched by submerging the vessel in room temperature water, vented to atmospheric conditions, and then centrifuged at 6000 rpm for 6 minutes before a 0.5 mL sample was taken for GC-FID analysis.

Gas chromatography (GC-FID) was performed using a Thermo Scientific Trace 1310 gas chromatograph with an SGE Analytical Science BP5 column (30 m × 0.25 mm × 0.25 μm). A 1.0 μL sample volume is injected at 300 °C, under constant pressure mode (25 psi), with a split flow of 90 mL and the following temperature profile: initial temperature 40 °C, ramp at 7.5 °C min^{-1} to 70 °C, ramp at 15 °C min^{-1} to 145 °C ramp at 45 °C min^{-1} to 280 °C and hold for 3 min. Species concentrations were determined *via* calibration curves (shown in ESI,† page S7) utilizing biphenyl as an internal standard. The molar turnover frequency (TOF_M) was calculated using conversion after 1 hour:

$$TOF_M = \frac{n_{BnOH}}{n_{Au} \cdot t} \quad (1)$$

where n_{BnOH} is moles of benzyl alcohol consumed, n_{Au} is total moles of gold from ICP-MS, and t is reaction time. This calculation does not specifically normalize by active site, but

is often referred to as turnover frequency in literature,[13,14,16,21,35,36] making it useful as a point of comparison when the nanoparticle sizes are similar. For more precise internal comparison, turnover frequency based on surface gold atoms was calculated for each catalyst:

$$\mathrm{TOF_s} = \frac{n_{\mathrm{BnOH}}}{n_{\mathrm{Au,s}} \cdot t} \quad (2)$$

where $n_{\mathrm{Au,s}}$ is the moles of gold atoms across the total surface area of the active phase in a given reaction. The method for calculating surface atoms is detailed in the ESI,† pages S8 and S9.

2.4.2 Kinetic analysis reaction conditions. A first-order initial rate approximation was verified in the first 30 minutes by performing a kinetic profile at 100 °C for 15, 30, 60, 120, and 240 minutes (as shown in ESI,† page S10). The activation energy was determined using the same reaction conditions but altering reaction temperature and holding reaction duration constant at 30 minutes. The experiment was carried out at 90 °C, 95 °C, 100 °C, 105 °C, 110 °C, and 115 °C.

2.4.3 Recyclability reaction conditions. Catalyst recyclability was determined for CSNPs using standard reaction conditions (*i.e.*, 100 °C for 1 hour). After quenching and centrifugation, a 0.5 mL sample was taken for GC-FID analysis. The vial containing the remaining solution was attached to a rotary evaporator and the solvent removed at 60 °C and a 67 mbar vacuum for 30 minutes or until the solvent was no longer visible. The species within the pores were removed *via* calcination, ramping 10 °C $\mathrm{min^{-1}}$ to 600 °C. The nanoparticles were removed from the oven and allowed to cool to room temperature. Once cooled, the same volume of stock solution was added and the reaction repeated.

3. Results and discussion

3.1 Nanoparticle characterization

TEM micrographs were obtained from collected samples at various points during the synthesis to provide insight into the formation of the encapsulating silica shell. TEM micrographs before the etching phase (*i.e.*, the second addition of TEOS and extended stirring period) are shown in Fig. 1A. By adjusting the focal length, pores in the silica are observable in the CSNPs before calcination, shown in Fig. 1B. Analysis of the size of the gold nanoparticles throughout the synthesis reaction demonstrate that Au nanoparticle nucleation, growth, and stabilization are rapid with respect to the formation of silica gel around the gold. These CTAB-stabilized gold nanoparticles, in addition to CTAB micelles,[37] act as a nucleation center for the growth of the silica. The gold nanoparticles have a diameter (d) of 5.2 ± 1.8 nm prior to the silica etching and increase after the completion of the synthesis and after calcination to 8.0 ± 3.9 nm, shown in Fig. 1C. The silica shells roughly quadruple in thickness during the growth/etching phase from 6.2 ± 1.8 nm to 27.4 ± 5.6 nm.

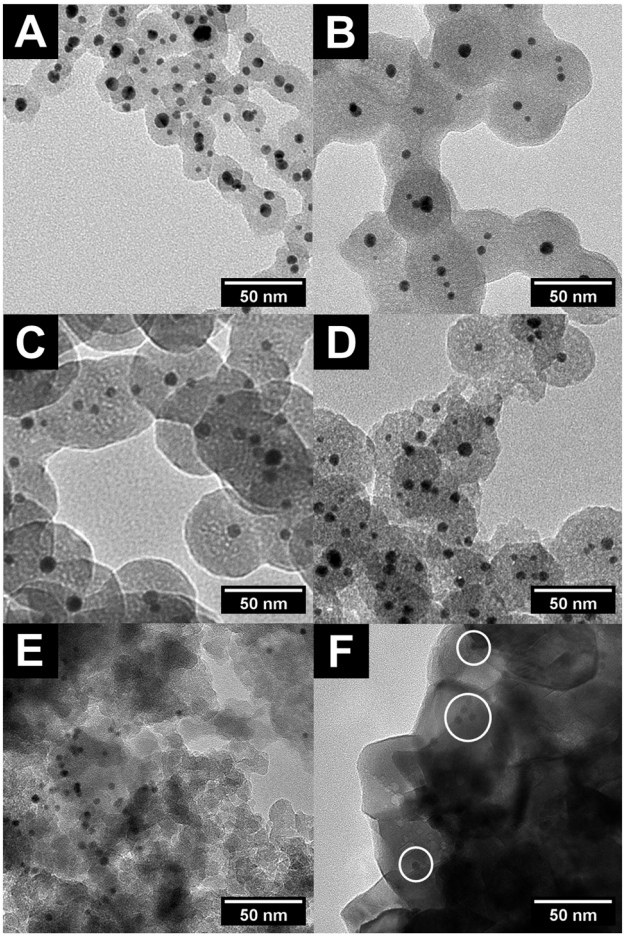

Fig. 1 TEM micrographs of Au@SiO_2 CSNPs and control catalysts. (A) CSNPs before the second addition of TEOS and subsequent etching phase. (B) CSNPs pre-calcination. (C) CSNPs post-calcination. (D) CSNPs after two sequential 1 hour benzyl alcohol oxidation reactions with no added base. (E) Silica-supported nanoparticles. (F) Ceria-supported nanoparticles.

Fig. 2 shows core diameter and shell thickness distributions (n = 402 gold cores, n = 188 silica shells counted), with morphology histograms of all samples are available in the ESI,† page S11. Typically, gold nanoparticles are encapsulated by the silica with rare occurrences of partially encapsulated gold nanoparticles. TEM images of both control catalysts after calcination are shown in Fig. 1E and F. Gold nanoparticles are visible on the surface of the silica and ceria supports. The average gold nanoparticle diameter was 8.4 ± 2.9 nm for the Au–SiO_2 nanoparticles and 6.1 ± 2.7 nm for the Au–CeO_2 nanoparticles, roughly on the same scale as the average CSNP core diameter to eliminate potential particle-size effects.

Digestion of the CSNP catalyst by aqua regia and analysis by ICP-MS determined that the catalyst was composed of 0.22% gold by mass. The Au–SiO_2 and Au–CeO_2 control catalysts were 0.055% and 0.10% gold by mass respectively. An estimate for surface atom ratio for each catalyst using both the nanoparticle size distribution and ICP-MS results is presented in Table 1.

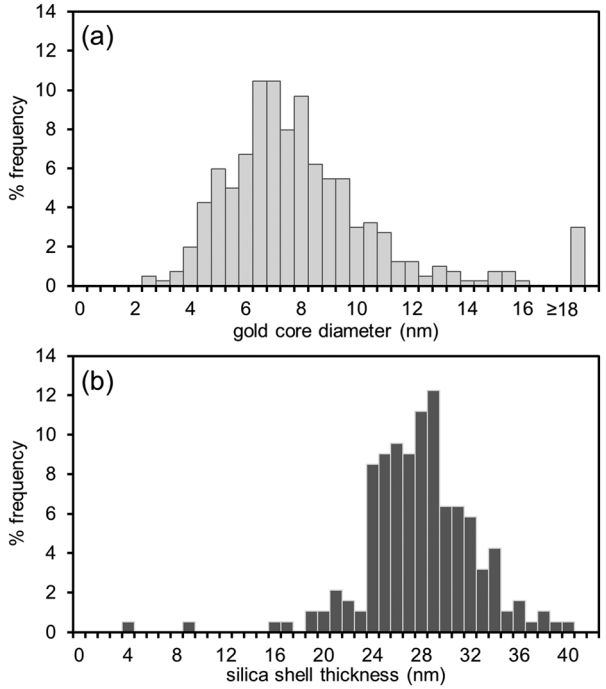

Fig. 2 (a) Gold core diameter histogram (n = 402) of post-calcination Au@SiO_2 CSNPs. d = 8.0 ± 3.9 nm (b) silica shell thickness histogram (n = 188) of the same sample. T = 27.4 ± 4.6 nm.

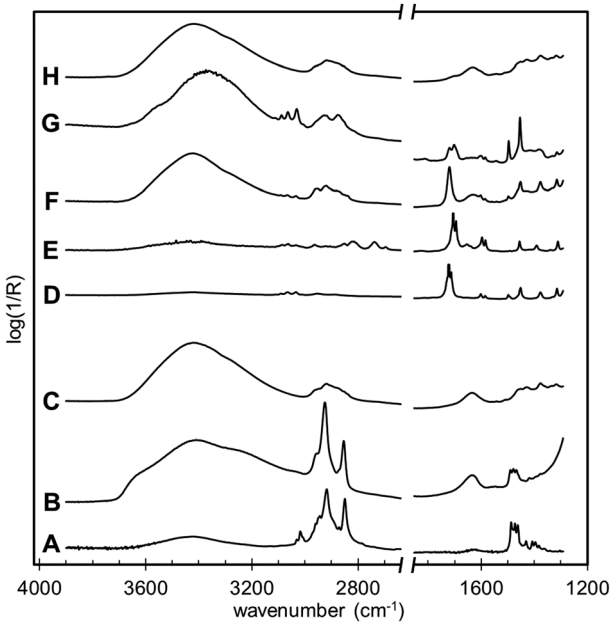

Fig. 3 Transmission FTIR of reaction species and CSNPs. (A) CTAB standard. (B) Pre-calcined CSNPs. (C) Calcined CSNPs. (D) Benzyl benzoate standard. (E) Benzaldehyde standard. (F) Benzyl alcohol standard. (G) CSNPs, calcined then once used. (H) CSNPs, calcined, once used then calcined again to remove reaction species from pores.

TGA-MS revealed pre-calcination core–shell nanoparticles lost 19.5% of their mass as combusted CO_2 and water (results available in ESI,† page S12). The nanoparticle synthesis requires a passivation layer of CTAB to stabilize the nanoparticles and provide a nucleation site for silica shell condensation. Additionally, partial hydrolysis of TEOS leaves residual ethoxy imperfections in the silica shell.[38] As such, the 19.5% wt loss can be attributed to a mixture of CTAB which is present after washing and drying, embedded ethylsilicate groups, and any ethanol remaining after the cleaning process. Similarly, Au–SiO_2 nanoparticles lost 13.6% of their mass, whereas Au–CeO_2 nanoparticles lost 0.8%. In both cases, the lost mass is due to the removal of silylamine on the support surface, with the difference in mass lost attributable to each support's relative affinity towards the silane.

FTIR spectra of relevant samples are shown in Fig. 3. Signals below 1300 cm^{-1} containing the Si–O bonding groups have been omitted for clarity. Comparison of the pure CTAB spectra (3A) to the pre-calcination CSNPs (3B), specifically the methylene scissoring[39] peak at 1500 cm^{-1} and the aliphatic peaks centered at 2900 cm^{-1}, confirms the existence of CTAB within the pores. These peaks are significantly reduced in the post-calcination spectra (3C), further evidence the calcination procedure is sufficient to clear CTAB from the silica structure. A residual peak centered at 2900 cm^{-1} in the calcined sample is attributable to aliphatic imperfections within the silica from the Stöber process.

Pre-calcination nanoparticles display a bimodal micro/mesopore distribution shown in Fig. 4, with peaks at 14 Å and 27 Å. Pore size distribution of calcined nanoparticles reveals a single peak with an average diameter of 30.9 Å, also shown in Fig. 4. Contextualized with the TGA-MS and FTIR results indicating the presence of CTAB in the as-synthesized pores, the small diameter peak of the pre-calcined CSNPs appears to represent partially-filled pores containing CTAB.

Table 1 Gold nanoparticle diameter, loading, and surface fraction for all catalysts synthesized

Catalyst	Nanoparticle diameter (nm)	Gold loading (wt%)	Surface atom fraction (%)
CSNPs	8.0 ± 3.9	0.22%	11.5%
Au–SiO_2	8.4 ± 2.9	0.055%	11.0%
Au–CeO_2	6.1 ± 2.7	0.10%	12.5%

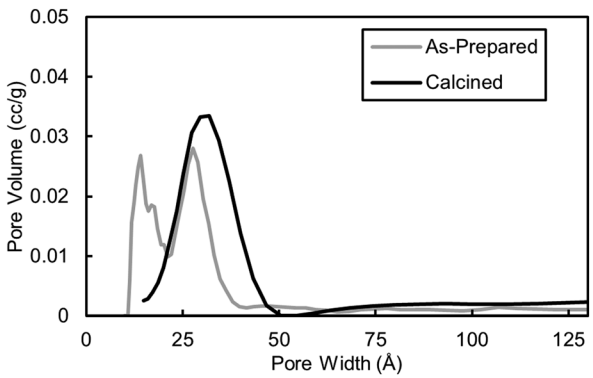

Fig. 4 Pore size distribution of as-prepared and calcined Au@SiO_2 core–shell nanoparticles.

The removal of CTAB through calcination will increase the apparent diameter and volume of these pores by freeing room for nitrogen, shifting the smaller peak upwards in diameter, forming a single, larger peak.

Rietveld refinements of XRD patterns (available in ESI,† Fig. S1) indicate a 2% increase in the gold lattice parameter is needed to fit the data compared to that of bulk gold, which is expected for gold nanoparticles.[40] Crystal domain sizes (available in ESI,† Table S1) generally show correlation with nanoparticle size as determined by TEM.

3.2 Catalytic performance results

3.2.1 Conversion/selectivity performance. Core–shell nanoparticles show high activity and selectivity towards benzaldehyde without an added base, as shown visually in Fig. 5. For comparison to control catalysts, a turnover frequency was calculated for all reactions in Fig. 5 using a surface atom basis. This data is presented in Table 2. Normalizing by surface atoms slightly improves the relative performance of Au–SiO_2 and is slightly detrimental to Au–CeO_2. This is as expected, given the difference in nanoparticle diameters. The high molar TOF of 3666 h^{-1} (surface TOF = 31 943 h^{-1}) in the absence of a base exceeds literature studies in similar environments, matching typical performance of a base-assisted reaction.[13] The core–shell nanoparticles showed a near-quantitative selectivity towards benzaldehyde in the absence of a base, agreeing with most literature studies which show high selectivity on gold when conversion is low.[12,41] The addition of a base is expected to increase the activity of the catalyst to the detriment of selectivity.[13] Addition of K_2CO_3 increased conversion from 17.3% to 60.4% (TOF_M = 12 814 h^{-1}, TOF_S = 111 652 h^{-1}) while the benzaldehyde selectivity decreased from 98.4% to 75.0%. Using equivalent gold mass with similar gold nanoparticle sizes, the control catalysts demonstrated negligible reactivity in the absence of a base. The conversion using Au–SiO_2 nanoparticles increased to 10.5% conversion (TOF_M = 2216 h^{-1}, TOF_S = 20 171 h^{-1}) in the presence of K_2CO_3, while the conversion using Au–CeO_2 nanoparticles increased to 4.7% (TOF_M = 999 h^{-1}, TOF_S = 8004 h^{-1}). Both with and without a base, CSNPs outperform the control catalysts by a wide margin. In all cases, conversion below 20% demonstrated near-quantitative selectivity, showing agreement with literature consensus.

Table 2 Turnover frequencies on a molar and surface atom basis for benzyl alcohol oxidation in the absence and presence of a base, on multiple gold nanoparticle catalysts

Reaction	Base	TOF_M (h^{-1})	TOF_S (h^{-1})
CSNPs	N.B.[a]	3666	31 943
Au–SiO_2	N.B.[a]	38	346
Au–CeO_2	N.B.[a]	41	329
CSNPs	K_2CO_3	12 814	111 652
Au–SiO_2	K_2CO_3	2216	20 171
Au–CeO_2	K_2CO_3	999	8004

[a] N.B. = no base added. Reactions conducted at 100 °C, 1 h.

It is important to note that the results in Fig. 5 speak to the fundamental activity, but not the fundamental selectivity, of each catalyst. The nature of thermodynamically favorable reactions in series inherently leads to a decrease in selectivity towards intermediate products at higher conversions. As a result, the differences in conversion make selectivity comparison using Fig. 5 alone less beneficial.

To investigate fundamental selectivity between the catalysts, comparisons must be made at similar conversions. To achieve this, reaction times using Au–SiO_2 and Au–CeO_2 nanoparticles with K_2CO_3 were increased to roughly match the conversion using CSNPs, also in the presence of K_2CO_3. The results summarized in Fig. 6. Conversion on CSNPs after reacting for 0.5 hours was used as the baseline. Au–SiO_2 nanoparticles took 3 hours to surpass the conversion benchmark while Au–CeO_2 nanoparticles took 8 hours. CSNPs and Au–CeO_2 nanoparticles exhibit comparable selectivity towards benzaldehyde (81.8% and 88.2%

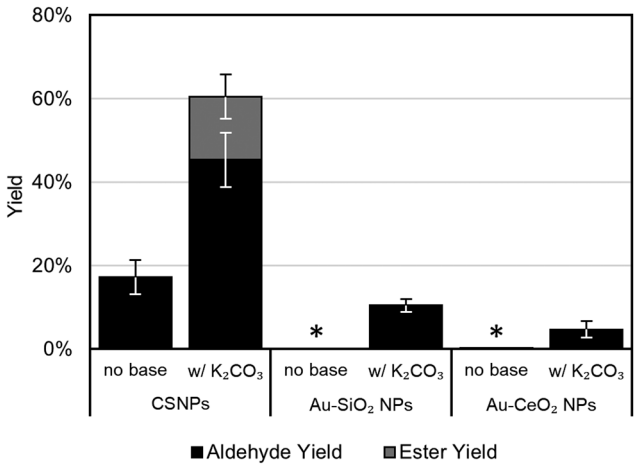

Fig. 5 Conversion and benzaldehyde selectivity of benzyl alcohol oxidation catalyzed by CSNPs and supported Au nanoparticles, with and without K_2CO_3. Asterisks denote negligible conversion.

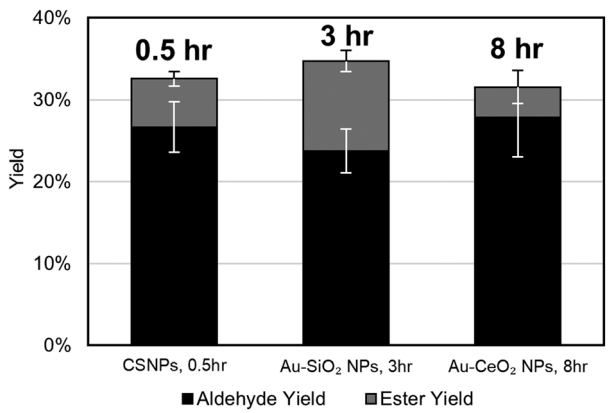

Fig. 6 Selectivity of benzyl alcohol oxidation catalyzed by CSNPs and supported Au nanoparticles, in the presence of K_2CO_3, reacted for decreasing times to match conversion on ceria-supported NPs.

respectively), both outperforming Au–SiO_2 nanoparticles (68.3%). Recent literature suggests ceria-supported nanoparticles maintain high selectivity due to strong metal–support interactions (SMSI). These interactions increase the oxidation state of atoms near the ceria surface to Au^{+1} from their ground state.[14,15] This beneficial interaction is the reason for their inclusion in this study, to provide a benchmark catalyst that receives measurable catalytic benefits from an interacting support material.

In this context, two clear benefits of CSNPs become apparent through Fig. 5 and 6. Firstly, CSNPs are fundamentally more active than both control catalysts by a wide margin. Secondly, CSNPs, which use a non-interacting support material, are fundamentally more selective than Au–SiO_2 and show comparable selectivity to a catalyst that maintains its selectivity through beneficial SMSI.

While Au–CeO_2 nanoparticles can achieve comparable selectivity given time in this case, their low activity made comparison at higher baseline conversions impossible. A separate attempt to match conversion on CSNPs after 1 hour (60.4% conversion) was performed, but Au–CeO_2 nanoparticles failed to reach the benchmark given 24 hours to react. Au–SiO_2 nanoparticles, taking 6 hours to reach the higher conversion benchmark (68.3%), showed only 49.4% selectivity towards benzaldehyde compared to 75.0% using CSNPs. Specific results can be found in the ESI,† page S13.

The unique behavior of the CSNPs compared to Au–SiO_2 NPs (*i.e.*, the maintenance of selectivity in the presence of a base) can be explained by the pore size distribution of the inert silica shell. The pore diameter is on the same scale as the molecular diameter of the reaction species, which exist roughly in the 5 to 9 Å region. The small pore sizes can leverage physical constraints to limit formation of larger products like benzoic acid and benzyl benzoate, maintaining a high selectivity in alkaline conditions that would otherwise drive the species to oxidize further. This is supported by the GC-FID results, as benzyl benzoate is present in only small quantities and benzoic acid was not detected. The combination of remarkable reactivity and selectivity using a catalyst confined within a mesoporous support is of particular interest; further investigation of catalysis in physically confined environments is underway.

3.2.2 Activation energy & mass transport. A 1st order Arrhenius analysis, shown in Fig. 7, was used to determine the activation energy of benzyl alcohol oxidation to benzaldehyde on all catalysts. No base was added to the reactions; this was done to ensure a single reaction step was occurring. The reaction conditions utilized yield only benzaldehyde, thus the measured activation energy is only for the conversion of benzyl alcohol to benzaldehyde. The calculated activation energy was 37 ± 1.9 kJ mol^{-1} using the CSNPs. This is small compared to other gold catalysts in literature.[41,42] It is also smaller than the control catalysts tested which had more typical values, 72 ± 7.1 kJ mol^{-1} using Au–SiO_2 nanoparticles and 63 ± 2.9 kJ mol^{-1} on Au–CeO_2 nanoparticles.

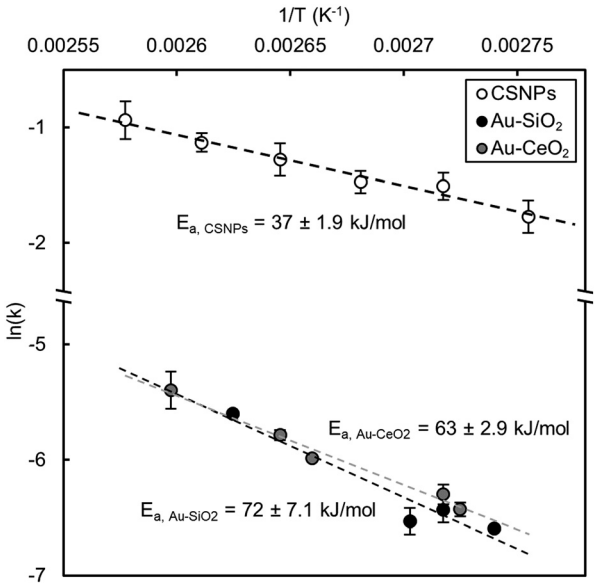

Fig. 7 Catalyzed benzyl alcohol oxidation Arrhenius plot for CSNPs and control catalysts, in the absence of a base.

Given the CSNPs require diffusion through pores to reach the active surface where the control catalysts do not; a lower activation energy may be reflective of a diffusion limitation. To determine whether diffusion limitation is responsible for the lowered activation energy, the Weisz–Prater parameter was calculated:[43]

$$C_{WP} = \frac{-r'_A(\text{obs})\rho_c R^2}{D_{eff} C_{As}} \quad (3)$$

where $-r'_A(\text{obs})$ is the observed rate of reaction per catalyst mass, ρ_c is the catalyst density when void volume is omitted, R is the silica shell thickness, and C_{As} is the concentration of benzyl alcohol at the catalyst surface. The reaction is well mixed; thus the surface benzyl alcohol concentration was assumed equal to bulk concentration. When $C_{WP} \ll 1$, diffusion is safely assumed negligible to catalytic performance.[44] The above equation assumes the catalytically active material is homogeneously distributed throughout the pellet, which is not the case for CSNPs. In cases with a longer path of diffusion or values close to the threshold, this discrepancy is worth considering.

To calculate the Weisz–Prater parameter, the effective diffusion coefficient is required:

$$D_{eff} = \frac{D_{bulk}\phi_p\sigma_c}{\tau} \quad (4)$$

where D_{bulk} is the bulk diffusion coefficient,[45] ϕ_p is the catalyst void fraction, σ_c is the porous constriction factor, and τ is the pore tortuosity. The parameters describing the pore structure (ϕ_p, σ_c, and τ) are based on morphology, meaning these values remain constant at different temperatures. They can thusly be combined into a single lumped parameter, determined by the ratio of empirical bulk diffusion and in-pore diffusion values. This value was calculated using studies

by Rottreau *et al.*,[46] who investigate diffusion of a variety of species within commonly available mesoporous silica structures. The diffusion of carboxylic acids within the random interconnected pores of KIT-6 silica most closely mirrored the CSNP structure. Bulk and effective diffusivity are presented in Table 3; example calculations for effective diffusivity are shown in the ESI† on page S14.

Given the small diameter of the catalyst pore, diffusing species will more frequently collide with the wall. When the mean free path of the particle approaches the pore diameter, the species enters the Knudsen diffusion regime, which can greatly inhibit diffusion depending on reaction conditions and catalyst morphology. It is well understood that species in mesopores diffuse in a regime between that of Knudsen and bulk diffusion, either forming intermittent liquid and gas phases within pores[47–49] or more simply a nebulous region where neither regime is fully accurate.[46,50–52] As such, it is valuable to calculate the Knudsen diffusion coefficients (D_{KA}) to determine the extent of this effect within CSNP pores at reaction conditions:

$$D_{KA} = \frac{d_P}{3}\sqrt{\frac{8RT}{\pi \cdot MW}} \quad (5)$$

where d_p is the average pore diameter (30.9 Å), T is the temperature, and MW is the molar mass of benzyl alcohol. Knudsen diffusivity values are presented in Table 3; example calculations are shown in the ESI† on page S14. At all points, the calculated Knudsen diffusion coefficient exceeds the bulk liquid diffusion coefficient and effective diffusion coefficient. This is to be expected in small pores at low temperatures,[53] as Knudsen diffusion is a form of inhibited gas diffusion.

With this, the effective diffusivity yields the lowest of all diffusivity values calculated, providing the least favorable estimate for diffusion limitation. Using the effective diffusion coefficients, the Weisz–Prater parameter was found to be $C_{WP} \approx 10^{-9} \ll 1$ at all temperatures (presented in Table 3). This is well beyond the threshold at which diffusion limitations are negligible. Example calculations for the Weisz–Prater parameter are shown in the ESI† on page S15.

A more common method to evaluate mass transport limitations is the Thiele modulus. Its ubiquity makes it easily understandable and useful as a rough point of comparison to other catalyst platforms. The temperature-dependent 1st order Thiele modulus (ϕ_{eff}) was calculated and presented in Table 3:

Table 3 Diffusivity values, Weisz–Prater parameters, and Thiele moduli using effective diffusivity for core–shell nanoparticle-catalyzed benzyl alcohol oxidation at various temperatures

	Diffusivity [$m^2\ s^{-1}$] × 10^{10}				
T [K]	Bulk	Knudsen	Effective	C_{WP}	ϕ_{eff}
363	4.39	2746	2.93	1.67×10^{-9}	1.10×10^{-5}
368	4.45	2765	2.97	2.12×10^{-9}	1.25×10^{-5}
373	4.51	2783	3.01	2.16×10^{-9}	1.26×10^{-5}
378	4.57	2802	3.05	2.56×10^{-9}	1.38×10^{-5}
383	4.63	2820	3.09	2.89×10^{-9}	1.48×10^{-5}

$$\phi_{eff} = R\sqrt{\frac{k}{D_{eff}}} \quad (6)$$

where R is the diffusion path-length (approximated by average silica shell thickness, 27.4 nm) k is the intrinsic rate constant at a given temperature, and D_{eff} is the effective diffusion coefficient of benzyl alcohol. The Weisz–Prater criterion indicates that our catalyst does not suffer from mass transport limitation, meaning the observed rate constant is the intrinsic rate constant. At all temperatures, the Thiele modulus indicates the reaction is rate-limited, agreeing with the Weisz–Prater criterion. Example calculations for the effective Thiele modulus can be found in the ESI† on page S14.

The small values for both C_{WP} and ϕ_{eff} can be primarily attributed to the short diffusion path, as $C_{WP} \propto R^2$ and $\phi_{eff} \propto R^1$. No matter the rate of diffusion, the nano-scale pore length is enough to overwhelmingly shift both parameters away from diffusion limitation to rate limitation. The distance from the pore entrance to the active surface is sufficiently small to not act as a barrier, even if diffusion is slow. This is true of all relevant reaction species, the effective diffusion coefficients necessary to counteract the short diffusion path would be several orders of magnitude lower than those calculated for benzyl alcohol. Barring significant differences in the mass transport mechanism between reaction species, changes of this magnitude are unlikely.

Given the reaction is not mass transport limited, the difference in activation energy must be due to a difference in mechanism on the respective metal surfaces. Fundamentally, there are two ways to achieve this effect: (1) by decreasing the activation energy of existing pathways, or (2) by promoting a lower activation energy mechanism among multiple pathways.

Low pore diameter could reduce the activation energy of a mechanism by promoting beneficial in-pore orientation. Dong *et al.*[54] use single-molecule measurements to demonstrate the effect of confinement on heterogeneous catalysis in pores ranging from 22 to 33 Å in diameter. Species under nanoconfinement within the pores were shown to orient favorably, ultimately resulting in higher catalytic activity. Given the small pore size of the CSNPs and benzyl alcohol's potential for beneficial orientation, it is plausible this effect plays a role in catalysis on CSNPs.

Furthermore, beneficial in-pore orientation could lead to a reduced apparent activation energy *via* a change in preferred mechanism, shifting the average activation energy towards a single, lower energy pathway. An analysis of the activation energies of various benzyl alcohol oxidation pathways on a bimetallic Au–Pd catalyst suggested the hydrogenolysis pathway to form benzaldehyde has an activation energy of 29.6 ± 6.6 kJ mol^{-1}.[55] This is roughly half the energy of the dehydrogenation pathway to benzaldehyde in the same system, while also being significantly smaller than the activation energies to form other oxidation products. In essence, a non-mechanistically selective catalyst would have a higher apparent activation energy than one a catalyst

selective towards the hydrogenolysis pathway. Despite the author's use of a bimetallic gold catalyst, similar pathways likely exist on a pure gold active site.

This appears to be the case when comparing the activation energies of the CSNPs and Au–SiO_2 nanoparticles, the only difference between the two being the catalyst geometry (*i.e.* the presence or absence of a mesoporous environment at the active surface). This indicates the low measured activation energy on CSNPs is due to the intrinsic reaction steps occurring on the catalyst surface, not the slowed transport of the reagent to the active surface through the pores. Absent other differences between the catalysts, it is likely the catalyst geometry influencing the apparent activation energy by limiting reagent orientation within the pores. Variation of pore size and shell thickness to further improve selectivity or select for different products is of particular interest, and preliminary research is underway to measure the impact of silica shell properties on diffusion in pores.

3.2.3 Recyclability performance. The catalyst was reused several times to determine the ability of the catalyst to be recycled after removing the solvent and products. The activity of the nanoparticles decreased on subsequent reuse as shown in Fig. 8, decreasing from 17.3% conversion to 5.8% (approximately 34% of initial reactivity) then remaining roughly constant for consecutive reuses. ANOVA analysis indicates cycles 2–4 are not statistically differentiable, but are all differentiable from the initial use. Despite the performance loss, the used catalyst demonstrates a consistently high reactivity, outperforming either control catalyst which show negligible activity in the solvent-free environment.

TEM analysis of the used CSNPs, as shown in Fig. 1D, indicates the decrease in reactivity could partially be due to nanoparticle aggregation (*i.e.*, decreased total surface area due to growth of nanoparticles), with the average particle size increasing slightly but significantly from 8.0 ± 3.9 nm to 8.7 ± 2.3 nm after two uses (*post hoc* Tukey HSD analysis).[56] The silica shell thickness decreased from 27.4 ± 4.6 nm to 19.2 ± 3.9 nm. Histograms of used nanoparticles can be found in the ESI,† page S11. This 9% increase in nanoparticle diameter, while statistically measurable, is not significant enough to fully explain the large performance loss.

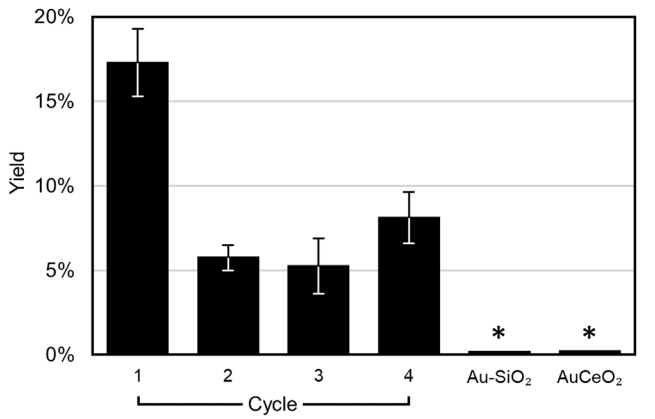

Fig. 8 Conversion and selectivity towards benzaldehyde of Au@SiO_2 core–shell nanoparticles over 4 consecutive uses, compared to first-use control catalysts.

To measure potential gold leaching, once-used CSNPs were separated from the reactant *via* centrifugation. The supernatant was collected, digested in 2 mL aqua regia, diluted and analyzed for gold content *via* ICP-MS. The gold detected in the supernatant corresponds to a 0.8% loss of gold mass from the catalyst into solution, far below the amount necessary to explain the decrease in performance between cycles 1 and 2.

FTIR analysis of once-used CSNPs (Fig. 3G) shows several signals absent in the calcined CSNPs signals prior to use. The doublet peaks at 1700 and 1720 cm^{-1} indicate a mixture of benzyl alcohol (3F), benzaldehyde (3E), and benzyl benzoate (3D). The balance of the two peaks within the CSNP pores shows no major deviation from the measured yields in the bulk solution. Importantly, the nanoparticles calcined after one-use show none of the peaks corresponding to benzyl species (3H). The spectrum is nearly identical to that of CSNPs before use, demonstrating the calcination procedure is sufficient to clear the pores of reaction species. There are several potential explanations for this apparent decrease in performance between the first and subsequent cycles, including surface rearrangements,[42] or agglomeration of unsecured or partially encapsulated gold, which would reduce size-specific reactivity of the active phase.

4. Conclusions

Core–shell Au@SiO_2 nanoparticles were synthesized *via* a bottom-up procedure, exhibiting enhanced selectivity due to the physical dimensions of the pore network, a phenomenon hereto unobserved for this structure. TEM investigation revealed the formation of a core–shell structure that is stable after multiple reactions. The nanoparticles catalyze solvent-free benzyl alcohol oxidation and exhibit high turnover frequencies compared to a chemically comparable control catalyst and a state-of-the-art catalyst exhibiting strong metal–support interactions. Alkaline conditions corresponding to the addition of K_2CO_3 increased reactivity while maintaining benzaldehyde selectivity much higher than control catalysts reaching the same conversion. The high selectivity can be attributed to a small silica pore diameter which inhibits the formation of larger, unfavorable benzoic acid or benzyl benzoate species. The high activity can be attributed to a nanoconfinement effect reducing the apparent activation energy. Furthermore, mass transport analysis suggests the catalytic system is not diffusion limited – therefore, the implementation of a thin encapsulating layer of mesoporous silica to control the orientation and transport of reagents is a promising technique to improve the activity and selectivity of aerobic oxidation catalysts.

Conflicts of interest

There are no conflicts to declare.

Acknowledgements

This work is supported through the National Science Foundation – Chemical, Biological, and Transport System Grant (CAREER – 1651597). Transmission electron microscopy was conducted at the Franceschi Microscopy & Imaging Center at Washington State University. E. H.-P. acknowledges support from the ARCS Foundation. T. R. G. acknowledges support from the Pacific Northwest National Laboratory – Washington State University Distinguished Graduate Research Program (PNNL-WSU DGRP) and partial support for X-ray diffraction from IDREAM (Interfacial Dynamics in Radioactive Environments and Materials), an Energy Frontier Research Center funded by the U.S. Department of Energy (DOE), Office of Science, Basic Energy Sciences (BES). X-ray diffraction used resources of the Advanced Photon Source, a U.S. DOE Office of Science User Facility operated for the DOE Office of Science by Argonne National Laboratory under Contract [DE-AC02-06CH11357], where data acquisition was performed at beam line 11-ID-B. D. W. acknowledges institutional funds from the Gene and Linda Voiland School of Chemical Engineering and Bioengineering and fund of the Alexandra Navrotsky Institute for Experimental Thermodynamics at Washington State University.

References

1 R. A. Sheldon and J. K. Kochi, *Metal-catalyzed oxidations of organic compounds: Mechanistic principles and synthetic methodology including biochemical processes*, Academic Press, New York, 012639380X edn, 1981.
2 M. Hudlicky, *Oxidations in organic chemistry*, American Chemical Society, 1990.
3 G. C. Bond, C. Louis and D. T. Thompson, *Catalysis by Gold*, Imperial College Press, London, 2006.
4 G. Tojo and M. I. Fernandez, *Oxidation of alcohols to aldehydes and ketones : a guide to current common practice*, Springer, New York, NY, 2006.
5 G. T. Brink, I. W. C. E. Arends and R. A. Sheldon, *Science*, 2000, **287**, 1636–1639.
6 D. J. Gorin, B. D. Sherry and F. D. Toste, *Chem. Rev.*, 2008, **108**, 3351–3378.
7 F. Fache, E. Schulz, M. L. Tommasino and M. Lemaire, *Chem. Rev.*, 2000, **100**, 2159–2231.
8 R. A. Sheldon, *Chem. Soc. Rev.*, 2012, **41**, 1437–1451.
9 L. Zhang, *Acc. Chem. Res.*, 2014, **47**, 877–888.
10 D. J. Cole-hamilton, *Science*, 2003, **299**, 1702–1707.
11 M. Davidson, Y. Ji, G. J. Leong, N. C. Kovach, B. G. Trewyn and R. M. Richards, *ACS Appl. Nano Mater.*, 2018, **1**, 4386–4400.
12 K. P. R. Castro, M. A. S. Garcia, W. C. de Abreu, S. A. A. de Sousa, C. V. R. de Moura, J. C. S. Costa and E. M. de Moura, *Catalysts*, 2018, **8**(2), 83.
13 C. P. Ferraz, M. A. S. Garcia, É. Teixeira-Neto and L. M. Rossi, *RSC Adv.*, 2016, **6**, 25279–25285.
14 M. Alhumaimess, Z. Lin, W. Weng, N. Dimitratos, N. F. Dummer, S. H. Taylor, J. K. Bartley, C. J. Kiely and G. J. Hutchings, *ChemSusChem*, 2012, **5**, 125–131.
15 A. Nozaki, T. Yasuoka, Y. Kuwahara, T. Ohmichi, K. Mori, T. Nagase, H. Y. Yasuda and H. Yamashita, *Ind. Eng. Chem. Res.*, 2018, **57**(16), 5599–5605.
16 G. Zhan, J. Huang, M. Du, D. Sun, I. Abdul-Rauf, W. Lin, Y. Hong and Q. Li, *Chem. Eng. J.*, 2012, **187**, 232–238.
17 V. R. Choudhary, A. Dhar, P. Jana, R. Jha and B. S. Uphade, *Green Chem.*, 2005, **7**, 768–770.
18 K. R. Seddon and A. Stark, *Green Chem.*, 2002, **4**, 119–123.
19 D. Obermayer, A. M. Balu, A. A. Romero, W. Goessler, R. Luque and C. O. Kappe, *Green Chem.*, 2013, **15**, 1530–1537.
20 M. Sankar, E. Nowicka, R. Tiruvalam, Q. He, S. H. Taylor, C. J. Kiely, D. Bethell, D. W. Knight and G. J. Hutchings, *Chem. – Eur. J.*, 2011, **17**, 6524–6532.
21 N. Dimitratos, J. A. Lopez-Sanchez, D. Morgan, A. Carley, L. Prati and G. J. Hutchings, *Catal. Today*, 2007, **122**, 317–324.
22 D. I. Enache, D. Barker, J. K. Edwards, S. H. Taylor, D. W. Knight, A. F. Carley and G. J. Hutchings, *Catal. Today*, 2007, **122**, 407–411.
23 S. Marx and A. Baiker, *J. Phys. Chem. C*, 2009, **113**, 6191–6201.
24 G. Zhao, F. Yang, Z. Chen, Q. Liu, Y. Ji, Y. Zhang, Z. Niu and J. Mao, *Nat. Commun.*, 2017, **8**, 1–8.
25 C. Y. Ma, B. J. Dou, J. J. Li, J. Cheng, Q. Hu, Z. P. Hao and S. Z. Qiao, *Appl. Catal., B*, 2009, **92**, 202–208.
26 M. Mahyari, A. Shaabani, M. Behbahani and A. Bagheri, *Appl. Organomet. Chem.*, 2014, **28**, 576–583.
27 J. Hu, L. Chen, K. Zhu, A. Suchopar and R. Richards, *Catal. Today*, 2007, **122**, 277–283.
28 Y. Liu, H. Tsunoyama, T. Akita and T. Tsukuda, *Chem. Lett.*, 2010, **39**, 159–161.
29 Y. Chen, Q. Wang and T. Wang, *Dalton Trans.*, 2015, **44**, 8867–8875.
30 A. L. Ethier, E. C. Hart, S. R. Saunders, E. J. Biddinger, A. Z. Fadhel, C. Dilek, P. Pollet, C. A. Eckert and C. L. Liotta, *Green Chem.*, 2014, **2**, 54–61.
31 K. Bryant, G. Ibrahim and S. R. Saunders, *Langmuir*, 2017, **33**, 12982–12988.
32 K. Bryant, C. W. West and S. R. Saunders, *Appl. Catal., A*, 2019, **579**, 58–64.
33 J. Landers, G. Y. Gor and A. V. Neimark, *Colloids Surf., A*, 2013, **437**, 3–32.
34 A. Hoeher, S. Mergelsberg, O. J. Borkiewicz and M. Patricia, *Acta Crystallogr., Sect. A: Found. Adv.*, 2019, **75**, 758–765.
35 Y. Chen, H. Lim, Q. Tang, Y. Gao, T. Sun, Q. Yan and Y. Yang, *Appl. Catal., A*, 2010, **380**, 55–65.
36 N. Dimitratos, J. A. Lopez-Sanchez, D. Morgan, A. F. Carley, R. Tiruvalam, C. J. Kiely, D. Bethell and G. J. Hutchings, *Phys. Chem. Chem. Phys.*, 2009, **11**, 5142–5153.
37 K. Ma, K. A. Spoth, Y. Cong, D. Zhang, T. Aubert, M. Z. Turker, L. F. Kourkoutis, E. Mendes and U. Wiesner, *J. Am. Chem. Soc.*, 2018, **140**, 17343–17348.
38 Y. J. Wong, L. Zhu, W. S. Teo, Y. W. Tan, Y. Yang, C. Wang and H. Chen, *J. Am. Chem. Soc.*, 2011, **133**, 11422–11425.
39 R. B. Viana, A. B. F. da Silva and A. S. Pimentel, *Adv. Phys. Chem.*, 2012, **2012**, 903272.
40 H. Nakotte, C. Silkwood, K. Page, H. Wang, D. Olds and B. Kiefer, *Phys. Scr.*, 2017, **92**(11), 114002–114012.

41 C. Della Pina, E. Falletta, L. Prati and M. Rossi, *Chem. Soc. Rev.*, 2008, **37**, 2077–2095.
42 M. Boronat, A. Corma, F. Illas, J. Radilla, T. Ródenas and M. J. Sabater, *J. Catal.*, 2011, **278**, 50–58.
43 P. B. Weisz and C. D. Prater, *Adv. Catal.*, 1954, **6**, 143–196.
44 H. S. Fogler, *Elements of Chemical Reaction Engineering*, 4th edn, 2005.
45 J. J. Chiu, D. J. Pine, S. T. Bishop and B. F. Chmelka, *J. Catal.*, 2004, **221**, 400–412.
46 T. J. Rottreau, C. M. A. Parlett, A. F. Lee and R. Evans, *J. Phys. Chem. C*, 2017, **121**, 16250–16256.
47 C. Carrara, G. Pag, C. Delaurent and S. Caldarelli, *J. Phys. Chem. C*, 2011, **115**, 18776–18781.
48 P. Zeigermann, S. Naumov, S. Mascotto, J. Karger, B. M. Smarsly and R. Valiullin, *Langmuir*, 2012, **28**, 3621–3632.
49 H. M. Alsyouri and J. Y. S. Lin, *J. Phys. Chem. B*, 2005, **109**, 13623–13629.
50 M. D. Mantle, D. I. Enache, E. Nowicka, S. P. Davies, J. K. Edwards, C. D. Agostino, D. P. Mascarenhas, L. Durham, M. Sankar, D. W. Knight, L. F. Gladden, S. H. Taylor and G. J. Hutchings, *J. Phys. Chem. C*, 2011, **115**, 1073–1079.
51 P. N. Sen, *Concepts Magn. Reson., Part A*, 2004, **23**, 1–21.
52 S. Reich, A. Svidrytski, A. Ho, J. Florek, F. Kleitz, W. Wang, C. Ku, D. Hlushkou and U. Tallarek, *J. Phys. Chem. C*, 2018, **122**, 12350–12361.
53 M. Hartmann, A. G. Machoke and W. Schwieger, *Chem. Soc. Rev.*, 2016, **45**, 3313–3330.
54 B. Dong, Y. Pei, N. Mansour, X. Lu, K. Yang, W. Huang and N. Fang, *Nat. Commun.*, 2019, **10**, 1–6.
55 F. Galvanin, M. Sankar, S. Cattaneo, D. Bethell, V. Dua, G. J. Hutchings and A. Gavriilidis, *Chem. Eng. J.*, 2018, **342**, 196–210.
56 J. W. Tukey, *Biometrics*, 1949, **5**, 99–114.